Preparation and structural characterization of ZnO and CeO$_2$ nanocomposite powders as 'active catalytic supports'

Celina E. Barrios [a], Miguel A. Baltanás [a,*], Raúl Bolmaro [b], Adrian L. Bonivardi [a]

[a] Instituto de Desarrollo Tecnológico para la Industria Química (Universidad Nacional del Litoral and CONICET), Güemes 3450, 3000, Santa Fe, Argentina
[b] Instituto de Física de Rosario (Universidad Nacional de Rosario and CONICET), Bvrd. 27 de Febrero 210 bis, 2000, Rosario, Argentina

ARTICLE INFO

ABSTRACT

Cerium(IV) and zinc(II) oxide nanocomposite powders (Zn-to-Ce atomic ratio between 0.5 and 2) as well as the pure oxides were prepared by co-precipitation of cerium(III) and zinc(II) cations with oxalate (OC) or carbonate anions (CC), as *active catalytic supports* for the steam reforming of methanol (SRM) reaction. After the study of the decomposition of the precipitates in oxidizing atmosphere by thermogravimetry, differential scanning calorimetry, temperature-programmed oxidation (using infrared and mass spectrometry) and X-ray diffraction, a global reaction pathway for the decomposition of each type of precipitates was proposed. The nanostructural characterization of the calcined composites at 723 K was followed by refined XRD analysis. It was possible to conclude that Zn(II) was not incorporated into the ceria lattice in any case. The size of the CeO$_2$ crystals was rather constant (~10–15 nm) in all the ZnO–CeO$_2$ nanocomposite powders, just as in the pure ceria (13–14 nm). Instead, the crystalline domains of ZnO were smaller in the nanocomposites than in pure zinc oxide (31–78 vs. 103–118 nm, respectively), and even smaller in the CC than in the OC materials (31–38 vs. 57–78 nm for CC vs. OC, respectively). Upon the incorporation of palladium to the oxides, to provide the metallic function on the catalysts, the carbonate-derived composites showed a better catalytic performance for the SRM reaction. Said improvement (in terms of percent selectivity to CO$_2$) could be attributed to the improved dispersion of zinc oxide achieved on the CC nanocomposites.

© 2014 Elsevier B.V. All rights reserved.

1. Introduction

The production of H$_2$ via the steam reforming of methanol (SRM) to feed fuel cells has been an object of several studies during the last two decades [1,2]. Copper-based catalysts, which are typically employed as Cu-Zn/Al$_2$O$_3$ formulations for the traditional synthesis of methanol, have also been used to that purpose. However, as these Cu-based materials present several drawbacks (e.g., copper sintering, self-ignition and ultimately, deactivation, among others), more recent work has been devoted to searching better materials. Among different alternatives, the 8–10 group catalysts seem to be the most promising [3]. In particular, the systems based on palladium and zinc have been highlighted by their remarkable selectivity to CO$_2$, which is attributed to the formation of ZnPd alloys or intermetallic compounds, while keeping a good yield to H$_2$ [2].

Nonetheless, *technological* catalytic materials involve complex compositions because the requirements that they must meet to achieve the best catalytic performance strongly depend on their end applications. In this regard, for instance, supported-Pd on pure ZnO has been found inappropriate to deal with the duty cycle to supply H$_2$ via SRM for portable fuel cells, because those power units have to be operated with recurrent start-up/shut-down sequences, where water condenses over the catalyst [4]. So, there is a compromise that rules the improvement of the materials' performance for this process where, for example, the enhancement of the selectivity to CO$_2$ must be balanced with the stability of the catalysts.

To this end, different supports have been used to improve the performance of the palladium–zinc system. The use of an inert support, such as black carbon, showed that Pd–ZnO/C was more stable than Pd/ZnO, but the catalyst deactivated after 40 h on stream a 523 K [5]. Alumina, meanwhile, has shown to be controversial in terms of stability [6,7] and, in addition, it has been associated to the detrimental dimethyl ether production as a by-product [8]. On the other hand, since the pioneering work of Iwasa et al. [9] it has been proved that the use of rare earth oxides increases both thermal stability and long-term catalytic stability of Pd–ZnO under SRM conditions, even above 673 K [10]. Thus, even though rare earth oxides have poor structural properties, a novel SRM material was developed recently at BASF Corporation Catalysts Division, consisting of palladium and zinc supported on yttrium-promoted ceria, which exhibited remarkable performance for this process [4,11,12].

Thereby, in an effort aiming to a better understanding of the Pd–ZnO/CeO$_2$ system, we present here the results of the preparation and characterization of two different series of ZnO–CeO$_2$ nanocomposite powders, which were also tested as 'active support materials' of Pd–based catalysts for the SRM reaction. This type of work is based on the need to achieve a good and economic ZnO anchoring method by improving the intimacy between the ZnO and CeO$_2$ phases while introducing, at the same time, hard restrictions in terms of purity and morphology of the solids. Naturally, these metal-oxide particulate materials must be later shaped into practical catalysts (e.g., so as to allow low pressure drop in fixed-bed reactors), with or without binders addition, by conventional pelletizing or kneading/extrusion techniques.

We selected two co-precipitation preparation methods which have shown to be able to produce powdered oxides of moderate surface area and, at the same time, we used decomposable compounds, to get rid of any residual ions or carbonaceous matter that could further interfere in the evaluation of the prepared materials for the SRM reaction. Ammonium carbonate was used as the first precipitating agent, because it can yield CeO$_2$ of moderate surface area whenever the initial concentration of Ce(III) cations is controlled [13]. In addition, coprecipitated oxalates were prepared by using a surfactant-free emulsion method, as described by He [14]. A detailed analysis of the thermal decomposition of these salts and the characterization of each set of ZnO–CeO$_2$ nanocomposite powders was then carried out, in as much as 'practical' catalytic materials can successfully be tailored only after a detailed understanding of the structure of their active constituents is achieved.

2. Materials and methods

2.1. Oxide powders preparation

Pure zinc and cerium oxides, and composite powders of both oxides containing different Zn/Ce = 0.5, 1 and 2 at/at ratios, were prepared using two alternate co-precipitation routes designated as OC (oxalates coprecipitation) and CC (carbonates coprecipitation), with further drying and calcining/decomposition in each case. The obtained materials were labeled indicating the preparation method (OC or CC), metal cation(s) and/or Zn/Ce atomic ratio (Ce, Zn, Zn/Ce) and further drying (D) and calcining (C) treatments. For comparison purposes, a third (conventional) type of composite powder, in which ZnO was incorporated on the surface of pure ceria by incipient wetness, was also included. This material type was designated as OI.

2.1.1. OC preparation method

A 0.34 M solution of dimethyloxalate (DMO) in 1-hexanol was added to aqueous solutions of cerium and/or zinc nitrates, using either the pure salts or their mixtures so as to get the desired Zn/Ce atomic ratio, but keeping always the same total cation concentration (0.04 M), under vigorous stirring (1000 rpm), at 313 K. The water to 1-hexanol ratio was always 2.5 v/v, while the molar DMO/(Ce^{3+} + Zn^{2+}) ratio was 3.2. The final volume of each preparation was approximately 1000 ml. The emulsions were stirred at 313 K for 1 h, after which they were slowly heated (heating rate, $\beta = 1$ K min^{-1}) to 333 K, and then left to stand still for another 2 h.

2.1.2. CC preparation method

Aqueous solutions of cerium and/or zinc nitrates (0.02 M) were stirred at 600 rpm for 1 h under CO$_2$ bubbling (30 ml min^{-1}), at room temperature (RT). Next, a 0.75 M solution of ammonium carbonate was added drop wise, with constant pH monitoring, until the final pH was 7.0–7.5.

The precipitates (OC or CC) were filtered using 0.2 μm nylon membranes and washed 10 times with small portions (10 ml each) of distilled water. Both precipitation methods gave about the same yield (>95%), as measured by atomic absorption.

The cakes were dried in a vacuum stove at 323 K for 30 h and then calcined in a glass reactor, at 723 K, during 4 h ($\beta = 3$ K min^{-1}) under a synthetic air flow O$_2$ (20%)/N$_2$ (W/F = 10^{-3} g h ml^{-1}). The calcined materials (oxides) were carefully ground and stored in a dessicator for further use.

2.1.3. OI preparation method

An aqueous solution of zinc nitrate was incorporated by incipient wetness to the dried and calcined CeO$_2$ previously obtained by oxalate precipitation, so as to get nominal ZnO coverage equal to 0.42 and 1.2 monolayers (3.5 and 11 wt% ZnO, respectively). Both materials were then dried in vacuo (393 K, 4 h) and calcined in the glass reactor using synthetic air at 673 K for 2 h ($\beta = 3$ K min^{-1}, from RT to 673 K).

2.2. Catalytic materials preparation

Palladium (2 wt%) was incorporated on the different (OC and CC) calcined powders by incipient wetness impregnation of acetone-diluted Pd(AcO)$_2$. On the OI supports, only 1 wt% Pd was added instead. After vacuum drying (333 K, 2 h), the impregnated catalyst precursors were calcined in the glass reactor using synthetic air at 673 K for 2 h ($\beta = 3$ K min^{-1}, from RT to 673 K). The materials, basically PdO on the surface of the oxides, were then crushed and sieved keeping the 40/80 mesh fraction, and stored in the dessicator, prior to their use.

2.3. Materials' characterization

The dry precipitates (support precursors), supports and catalysts were characterized in detail using the following techniques.

2.3.1. Thermogravimetry (TG) and differential scanning calorimetry (DSC)

Approximately 2.5 mg of each dry precipitate was placed into aluminum crucibles (with perforated lids). Its calcination or decomposition in synthetic air was followed in TG/SDTA (Mettler-Toledo, model 851e) and DSC (Mettler-Toledo, model 821e) units, under dynamic conditions ($\beta = 10$ K min^{-1}, O$_2$(20%)/N$_2$ (100 ml NTP min^{-1}), within the 298–973 K (TG) and 298–723 K (DSC) ranges, respectively.

2.3.2. X ray diffraction

The dried (323 K), partially decomposed (at 473 K) and air-calcined (at 723 K) powders were studied using CuKα radiation (30 kV and 40 mA), in a Shimadzu model XD-D1 diffractometer, with a scan speed of 2° 2θ min^{-1}. A slow scan (0.125° 2θ min^{-1}) was also done between the 26 < º2θ < 31 range – that is, around the (111) plane of CeO$_2$ – in selected calcined materials, namely: OC-Ce, CC-Ce, OC-ZnCe1 and CC-ZnCe1.

More detailed crystallographic information about the calcined powders was obtained using a Panalytical MPD unit equipped with a Cu anode, X-ray lenses, Xe gas detector, graphite monochromator and Soller parallel plates on the secondary beam. Measurements were made adding the Kα$_{1,2}$ signals, with vertical and horizontal slits (3 × 3 mm^2 beam area), in continuous scans (5 s per 0.02° 2θ increment) in the 20° < 2θ < 105° range. Data analyses were made by the Rietveld refinement technique, as implemented in the MAUD program [15–17]. A LaB$_6$ standard was used to estimate the instrumental peak broadening by calculating the Cagliotti coefficients and, then, the corresponding domain sizes by the Delf model. In every case, microdeformations were negligible (<10^{-4}).

2.3.3. Temperature programmed oxidation-infrared spectroscopy (TPO-IR)

Wafers of the dry precipitates (13 mm diameter, pressed to 2×10^4 N), diluted with dry KBr, were placed into a heatable Pyrex glass IR cell with refrigerated NaCl windows, attached to a conventional vacuum system (base pressure = 1.33×10^{-4} Pa) equipped with a manifold for gas flow. The cell temperature was varied between 298 and 723 K ($\beta = 5$ K min^{-1}) under a flowing O$_2$(20%)/N$_2$ (50 ml min^{-1}) mixture.

Transmission spectra were taken using a FTIR Nicolet Magna IR 550 Series II unit, furnished with a MCT-A detector (4 cm^{--} resolution, 64 scans per spectrum). A sum of Lorentzian and Gaussian function was used to solve overlapped bands, whenever needed.

2.3.4. Temperature programmed oxidation-mass spectroscopy (TPO-MS)

About 50 mg of selected samples, diluted with quartz, was placed between glass wool plugs inside a Pyrex lined stainless steel microreactor. Temperature was raised from 298 to 723 K ($\beta = 5$ K min^{-1}) in flowing $O_2(5\%)/He$ (50 ml min^{-1}). The exit gases were analyzed with a Balzers QMG-421 mass spectrometer, furnished with a SEM detector, monitoring the 44, 32, 28 and 18 m/e signals corresponding to CO_2, O_2, CO and H_2O, respectively. The 28 m/e signal was corrected to account for the CO_2 fragmentation.

2.3.5. Sorptometry

Sorption isotherms were measured at LN2 temperature (77 K), in a Micromeritics ASAP 2000 unit. Prior to measuring, the samples of the calcined materials were outgassed under dynamic vacuum (base pressure = 1.33×10^{-4} Pa) at 393 K for approximately 4 h. The specific surface area was estimated by the Brunauer–Emmett–Teller method (S_{BET}), using the data taken in the $0.05 < p/p_o < 0.3$ range. Pore size distribution was calculated with the Barrett–Joyner–Halenda (BJH) method, using the isotherm adsorption branch.

2.4. Catalysts' performance

An evaporated, equimolar mixture of CH_3OH and H_2O diluted in a He stream (8% v/v of each reactant) was fed to a thermostatized glass-lined stainless steel flow microrreactor (internal diameter = 3.5 mm), using about 50 mg of powdered catalyst. Inlet and exit gas compositions were measured by gas chromatography, using two Shimadzu 9A units (GC1 and GC2) operating in parallel. GC1 was used to quantify H_2O and CO_2 (TCD) and CH_3OH, CH_4 and $HCOOCH_3$ (FID), while CG2 was used to quantify CO, CO_2 and CH_4 (traces), using Porapak Q and Carbosieve SII packed columns.

Each catalyst was pretreated in situ, heating from 298 to 623 K ($\beta = 2$ K min^{-1}) under pure H_2 and maintaining this last temperature for 2 h. The reactor was then cooled to 398 K. The catalytic performance evaluation was done using 'temperature steps', from 398 to 623 K (1 h/each; $\beta = 1$ K min^{-1} between steps).

2.5. Reagents

High purity cerium and zinc nitrates, $Ce(NO_3)_3 \cdot 6H_2O$ (99.99% Ce), $Zn(NO_3)_2 \cdot 6H_2O$ (99.999% Zn), dimethyloxalate (99%), 1-hexanol (98%), $(NH_4)_2CO_3$ (ACS grade, $\geq$ 30% NH_3 basis) and $Pd(AcO)_2$ (99.97% Pd) were purchased to Sigma-Aldrich. Methanol (99.9%) was supplied by Merck. Water was tridistilled, Millipore grade (18 MΩ).

Ultra-high purity gases: He (99.999%), H_2 (99.998%), N_2 (99.999%), O_2 (99.999%), $O_2(5\%)/He$ (99.999%) and CO_2 (99.9%), were supplied by Indura (Air Products Argentina), and used as received without further purification.

3. Results and discussion

3.1. Oxalate method. Thermal evolutions of the oxalate precipitates

3.1.1. Mass, thermal and structural evolutions

Fig. 1 shows the combined results of TG and DSC analyses on representative samples of the oxalate precipitated powders. The corresponding X-ray diffractograms of the dry (323 K), partially decomposed (473 K) and calcined (723 K) materials are shown in Fig. 2.

Two mass evolutions were observed on the dry pure cerium(III) precipitate, OC-CeD, in the 350–410 K range (-17 wt% loss) and 550–660 K (-53 wt% loss), respectively (Fig. 1). The given figures
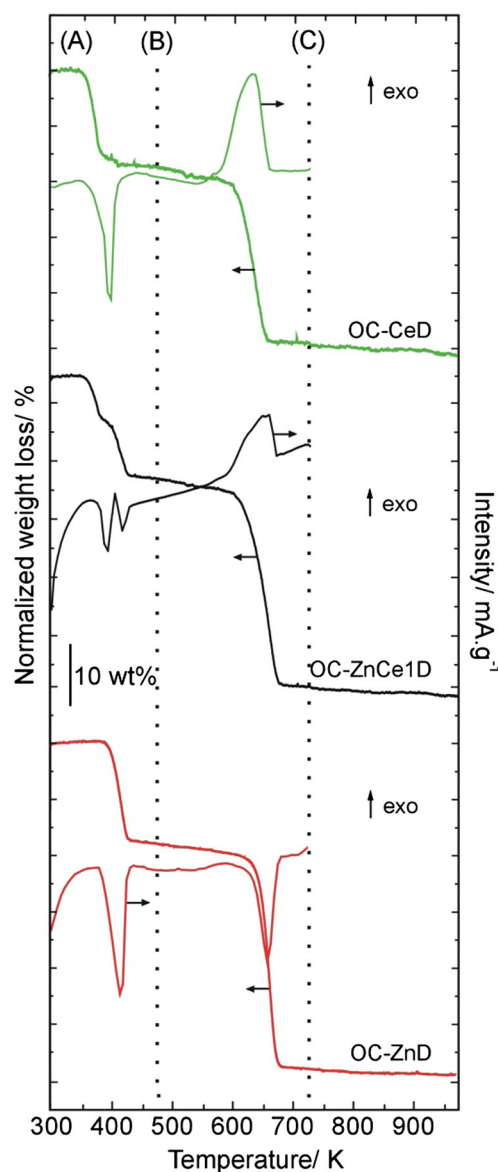

Fig. 1. Thermogravimetry and differential scanning calorimetry (TG and DSC) of the oxalate-precipitated (OC) powders, vacuum dried at 323 K: (—) OC-CeD, (—) OC-ZnCe1D, and (—) OC-ZnD.

are cumulative weight losses, that is, normalized to the initial weight of each sample. In the temperature regions corresponding to the weight loss steps, the DSC trace showed an endothermal peak (390 K), followed by an exothermal peak (625 K). The first evolution is associated with the release of crystallization water from $Ce_2(C_2O_4)_3 \cdot nH_2O$, with n ~ 6. The XRD of the cerium(III) oxalate hexahydrate shows intense signals at 2θ (percent relative intensity between parentheses) 18.3 (100%), 38.7 (22%), 29.1 (21%) and 48.1 (11%). As expected from the mass balance, the diffractogram of this hexahydrate differs from the ones corresponding to the dehydrated (JCPDS 40-570), nonahydrated (JCPDS 14-710) and decahydrated (JCPDS 20-268) cerium(III) oxalates.

After the water loss at 473 K amorphous cerium(III) oxalate was obtained, which, in turn, decomposed exothermally at 625 K to give CeO_2 (coded OC-CeDC hereafter), with cubic structure (JCPDS 4-593, see regions B and C in Fig. 2).

The dry pure zinc(II) precipitate (OC-ZnD) gave congruent mass and thermal signals as well, showing an absolute weight loss of – 18 wt% in the low temperature region (375–440 K), down to about – 58 wt%
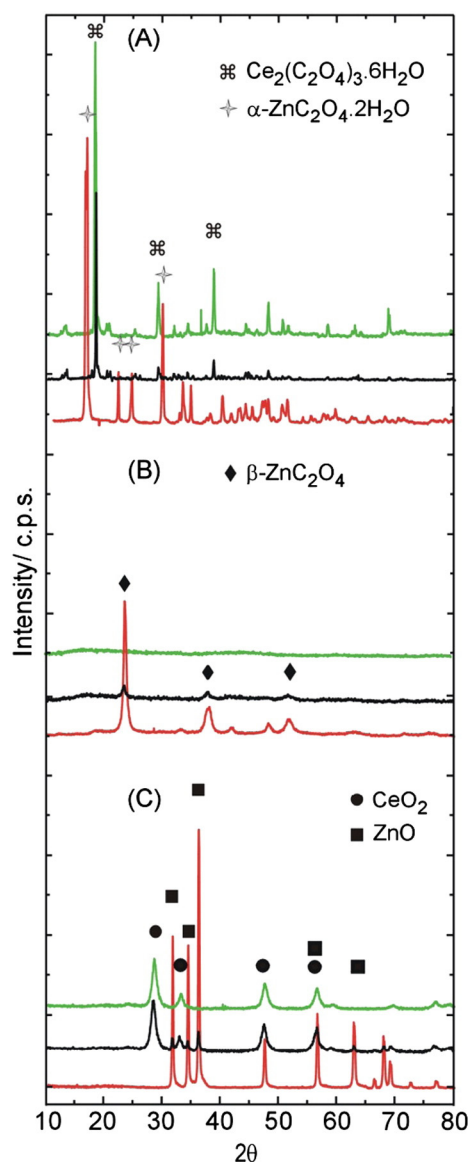
Fig. 2. X-ray diffractograms of the oxalate-precipitated powders (━) OC-Ce, (━) OC-ZnCe1, and (━) OC-Zn: (A) dried at 323 K, (B) decomposed at 473 K, and (C) calcined at 723 K (under synthetic air).

in the high temperature one (625–690 K). Both processes were endothermal, with maxima at 410 and 663 K, respectively (Fig. 1).

The diffractogram of the dry powder was typical of α-ZnC$_2$O$_4$•2H$_2$O (JCPDS 25-1029), which decomposed into β-ZnC$_2$O$_4$ (JCPDS 37-718) at 473 K, as it is unambiguously shown in Fig. 2, region B. The decomposition of zinc(II) oxalate in air at 723 K led to ZnO (coded OC-ZnDC hereafter) with hexagonal (wurtzite) structure, JCPDS 5-664 (Fig. 2, region C).

The thermal decomposition of the dry oxalate-coprecipitated zinc and cerium powder (Zn/Ce = 1 at/at sample, coded OC-ZnCe1D) is shown in Figs. 1 and 2. Two consecutive endothermal processes could be appreciated (mass losses at 390 and 410 K), which correspond to the dehydration/decomposition of the Ce(III) and Zn(II) oxalates, respectively. The diffractogram of the dry sample (region A in Fig. 2) clearly puts into evidence that the precipitated cerium salt is Ce$_2$(C$_2$O$_4$)$_3$•6H$_2$O, but no signal attributable to ZnC$_2$O$_4$•2H$_2$O was observed, indicating that this last oxalate was either amorphous or very finely divided prior to the descomposition/calcining step.

The decomposition at 473 K of the mixture of hydrated oxalates led to a highly amorphous material, in which only the presence of

the β-ZnC$_2$O$_4$ could be appreciated, albeit with very weak peak intensity (region B, Fig. 2).

Further heating of the dehydrated oxalates produced an exothermal signal, smaller than from the pure cerium oxalate. This is compatible with the fact that the composite material contains less cerium than OC-CeD and that zinc oxalate decomposition (which occurred simultaneously) was endothermal (Fig. 1).

The dehydration/decomposition of the dry support precursors, followed by TPO-IR, showed the characteristic bands of oxalate anions and molecular water, in every case. The signals at 1364(m)/1368(vs), 1464(m)/1470(m), 1605(vs)/1603(vs) and 1639(vs)/1720(vs) cm^{-1} are assigned to the asymmetric stretching, ν_{as}, of the C$_2$O$_4^{=}$ anion in the cerium/zinc salts, respectively, while the 1313(vs) cm^{-1} band is assigned to the symmetric stretching of the anion, ν_s, in both cases [18, 19]. The bands located at 1630(w) and ~3410(vs, broad) cm^{-1} correspond to the deformation, δ, and stretching, ν, of the OH of crystallization water (see Fig. 1S in Supplementary Information).

After heating under synthetic air, the oxalate species progressively decomposed. Fig. 3 shows the thermal evolution of the normalized integrated area of the stretching signals of hydroxyl, ν(OH), and oxalate, $\nu_{as} + \nu_s$, located at ~1365 and 1313 cm^{-1}, respectively (the other ν_{as} bands overlap with the water δ(OH) signal). Clearly, the disappearance of the ν(OH) band indicates the loss of crystallization water of the oxalates in the 350–410 K range, while the oxalate anions decomposed above 550 K. No carbonate formation was detected, which implies that the decomposition of the oxalate anion proceeded without any re-adsorption/absorption of CO$_2$ or CO products. All these results are congruent with the TG, DSC and XRD evolutions previously shown.

3.1.2. Gaseous products from the support precursors upon heating (TPO-MS)

Fig. 4 shows the evolution of the H$_2$O, CO and CO$_2$ signals, as well as the oxygen consumption upon heating, of the dry OC precipitates. Water release (m/e = 18) was observed at T < 450 K in all of them. In particular, and in accordance with the TG and DSC results, the Zn/Ce composite showed two water peaks, corresponding to the sequential dehydration of the cerium(III) and zinc(II) oxalates, respectively.

The inspection of the m/e = 44 and 28 signals (CO$_2$ and CO) showed that OC-CeD decomposition produced only CO$_2$, whereas
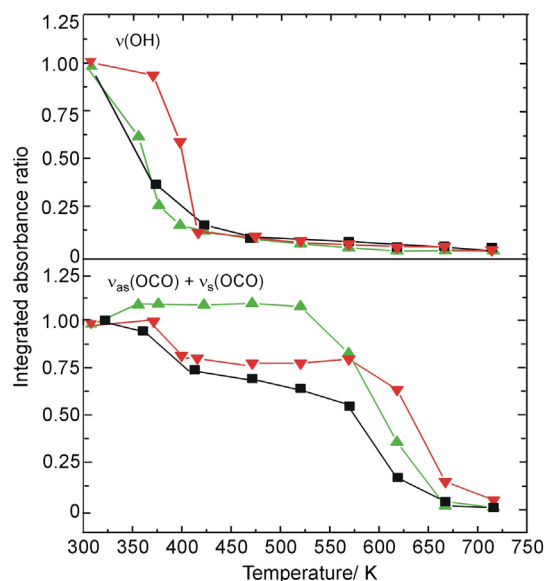
Fig. 3. Thermal evolution of the normalized integrated areas (transmission infrared) of the hydroxyl [ν(OH), ~3410 cm^{-1}] and oxalate [ν_s(OCO) + ν_{as}(OCO), 1313 + 1365 cm^{-1}] stretching bands of OC-CeD (▲), OC-ZnCe1D (■) and OC-ZnD (▼), during temperature programmed oxidation (TPO-IR).
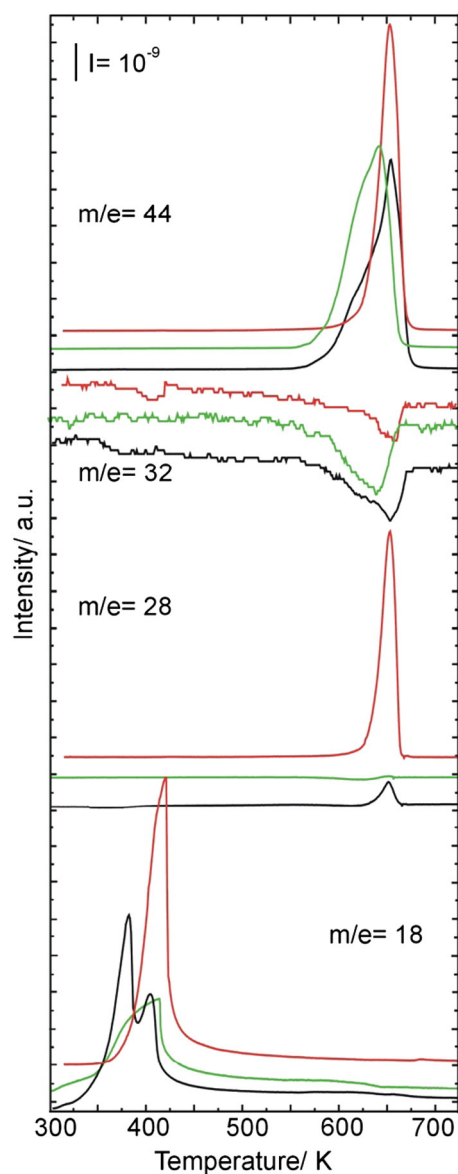
Fig. 4. Temperature programmed oxidation-mass spectroscopy (TPO-MS) patterns of the products of the OC materials under synthetic air: (——) OC-CeD, (——) OC-ZnCe1D, and (——) OC-ZnD.

OC-ZnD produced both gases, CO_2 and CO, in equivalent amounts. The composite material (OC-ZnCe1D) yielded 4-fold more CO_2 than CO, though.

Oxalates decomposition, at T > 550 K, was accompanied by O_2 consumption, with the subsequent oxidation of Ce(III) to Ce(IV) (see m/e = 32 in Fig. 4). Oxygen was also consumed by the OC-ZnCe1 sample, primarily due to Ce(III) oxidation. However CO oxidation also occurred, as the intensity of the CO signal was about 4-fold smaller than the one in OC-Zn, instead of the expected mass-normalized value (about half size). Most likely, the presence of cerium in the composite powder – and its facile uptake of oxygen – was the cause of this discrepancy.

Thus, from the combined analysis of the different thermal evolutions that were studied, the decomposition process of the materials prepared by the OC method in the oxidizing atmosphere can be summarized according to Scheme 1, shown below. Table 1 compares the experimental and theoretical weight losses of these OC-type supports, for the proposed decomposition scheme, showing an excellent agreement between them.

3.2. Carbonate method. Thermal evolutions of the carbonate precipitates

3.2.1. Mass, thermal and structural evolutions

The TG and DSC traces of dry, representative samples of this group of powders, prepared by precipitation as carbonate(s), are shown in Fig. 5. The respective changes in crystalline structure experienced by the materials dried at 323 K, air decomposed at 473 K and calcined at 723 K, are indicated in Fig. 6.

A first weight loss at 310–473 K (−18 wt%), followed by another one between 500 and 600 K (−40 wt%) was observed for the dry cerium precipitate (CC-CeD). The first weight loss is associated with three overlapped, endothermal processes (at 354, 371 and 428 K) while the second weight loss, also endothermal, proceeded with a DSC peak maximum located at ~550 K. The mass reduction measured below 473 K was assigned to the endothermal loss, in successive steps, of crystallization water of $Ce_2(CO_3)_3 \cdot nH_2O$ (n ~ 6), in agreement with the corresponding diffractogram, shown in the A region of Fig. 6 (JCPDS 30-295). After the water loss and above 475 K, the resulting, amorphous $Ce_2(CO_3)_3$, decomposed endothermally under the oxidizing atmosphere to give CeO_2 as the final product, with fluorite-type cubic structure (B and C regions in Fig. 6).

The pure, dry zinc precipitate (CC-ZnD), exhibited a diffractogram with peak positions and intensities belonging to either $Zn_5(CO_3)_2(OH)_6$ (JCPDS 14-256, hydrocincite), or $Zn_4CO_3(OH)_6 \cdot H_2O$ (JCPDS 11-287). However, after analyzing the H_2O and CO_2 signals during TPO-MS (see below), the latter crystal structure could be disregarded.
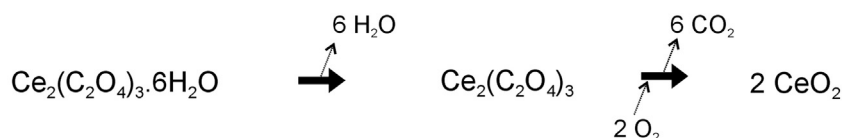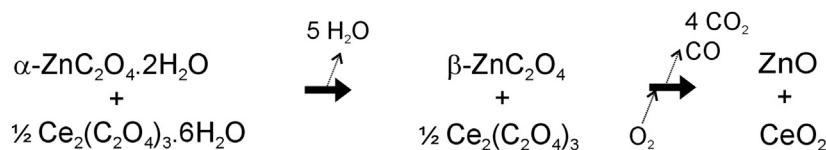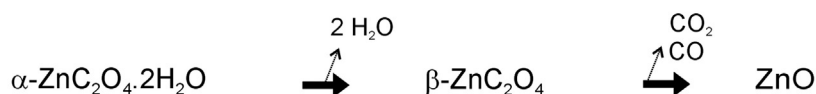
The zinc(II) hydroxycarbonate remained stable up to approximately 460 K, with a single endothermal decomposition step at ~510 K and a weight loss of −21 wt% in the 465–540 K range (Fig. 5), after which ZnO (wurtzite) was again obtained (C region of the XRD spectra, Fig. 6).

Unlike the pure cerium or zinc support precursors, the dry composite powder (CC-ZnCe1D) exhibited a diffractogram where only hexahydrated cerium carbonate could be identified, which revealed that the zinc salt was highly dispersed – or amorphous – into a cerium carbonate matrix. Fig. 5 shows that upon heating this composite suffered three weight losses, the first one (−11 wt%) in the 300–375 K range and the other two in the 430–600 K range (−18 wt% and −35 wt%, respectively). Coincidentally, the DSC trace indicated three endothermal evolutions, two of them with sharp, well resolved maxima at 370 and 470 K, and a broad smooth one between 510 and 650 K.

The first evolution was assigned to the dehydration of $Ce_2(CO_3)_3 \cdot 6H_2O$ which, at variance with what was observed on the pure ceria (CC-CeD), only occurred in a single step and at an intermediate temperature (382 K) between the convoluted peaks shown in the DSC trace of CC-CeD. It is highly feasible, then, that the environment of the hydrated cerium carbonate was modified by the fine, amorphous particles of the zinc salt.

The following thermal evolution of CC-ZnCe1D is consistent with the decomposition of zinc hydroxycarbonate because, as shown below (TPO-IR and TPO-MS results), part of the carbonates, and water, was released there. The outcome of the decomposition at 473 K gave an amorphous powder (B region, Fig. 6). Finally, the last, oxidative decomposition along the broad temperature range suggests that the carbonates decomposition of this sample produced a material substantially different from the one that would have been obtained by simply adding (mechanical mixture) the dry cerium and zinc pure salts using the same Zn/Ce = 1 ratio. Diffraction peaks corresponding to fluorite-type CeO_2, and (very weak) peaks corresponding to ZnO (wurtzite) were identified, but their peak intensity ratio indicated that the latter was less crystalline (or more amorphous) than in the equivalent (viz., Zn/Ce = 1) composite prepared via the OC method. Therefore, it is highly likely that the nucleation and/or growth processes of ZnO during the decomposition of the cerium(III) hydroxycarbonate were modified, leading to a lower crystallinity of the zinc oxide.

The TPO-IR spectra of the CC-CeD precursor showed characteristic carbonate bands, located at 1080, 1330, 1370 y 1488 cm^{-1} (see Fig. 2S

OC-CeD

$$Ce_2(C_2O_4)_3 \cdot 6H_2O \xrightarrow{\;6\;H_2O\;} Ce_2(C_2O_4)_3 \xrightarrow[\;2\;O_2\;]{\;6\;CO_2\;} 2\;CeO_2$$

OC-ZnCe1D

$$\begin{array}{c} \alpha\text{-}ZnC_2O_4 \cdot 2H_2O \\ + \\ \tfrac{1}{2}\,Ce_2(C_2O_4)_3 \cdot 6H_2O \end{array} \xrightarrow{\;5\;H_2O\;} \begin{array}{c} \beta\text{-}ZnC_2O_4 \\ + \\ \tfrac{1}{2}\,Ce_2(C_2O_4)_3 \end{array} \xrightarrow[\;O_2\;]{\;4\;CO_2,\;CO\;} \begin{array}{c} ZnO \\ + \\ CeO_2 \end{array}$$

OC-ZnD

$$\alpha\text{-}ZnC_2O_4 \cdot 2H_2O \xrightarrow{\;2\;H_2O\;} \beta\text{-}ZnC_2O_4 \xrightarrow{\;CO_2,\;CO\;} ZnO$$

Scheme 1. Global reaction pathway of the OC-precipitates.

in Supplementary Information). The first one was assigned to the symmetric stretching, ν_s, and the remaining ones to the asymmetric stretching, ν_{as}, of the C–O bonds of the $CO_3^=$ ion [19–21]. The band at 1640 cm^{-1} was again assigned to the $\delta(OH)$ of water in $Ce_2(CO_3)_3 \cdot 6H_2O$, together with an accompanying, broad band between 2700 and 3700 cm^{-1} due to the $\nu(OH)$ vibration mode.

The CC-ZnD precursor also exhibited the typical $CO_3^=$ spectral bands, located at 1048, 1347, 1380 and 1520 cm^{-1}. Recently, Hales and Frost gave a detailed characterization of hydrozincite [$Zn_5(OH)_6(CO_3)_2$] and smithsonite ($ZnCO_3$) [21]. From their results, the 1048 cm^{-1} band was assigned to $\nu_s(CO_3)$, and the remaining bands to $\nu_{as}(CO_3)$. Again, the 1630 cm^{-1} was ascribed to the δ vibration of the OH groups of zinc hydroxycarbonate, whose stretching mode, ν, was observed in the 2700–3700 cm^{-1} region.

The dry composite powder, CC-ZnCe1D (Zn/Ce = 1), gave an infrared spectrum closer to CC-CeD than to CC-ZnD. This is coherent with the fact that the anion ($CO_3^=$ and OH$^-$) to metal cation ratios are much higher in $Ce_2(CO_3)_3 \cdot 6H_2O$ ($CO_3^=$/Ce = 3/2 and OH$^-$/Ce = 6) than in hydrozincite ($CO_3^=$/Zn = 2/5 and OH$^-$/Zn = 6/5), respectively. The thermal evolution of the normalized integrated absorbance of the $CO_3^=$ and OH$^-$ groups is shown in Fig. 7. All these traces indicate progressive dehydration (more delayed in CC-ZnD), and carbonate decomposition below 600 K, in agreement with the TG and DSC data. The decomposition of $Ce_2(CO_3)_3 \cdot 6H_2O$ up to 473 K leads first to carbonates, which decomposed later, above 550 K. In hydrozincite, $Zn_5(OH)_6(CO_3)_2$, water and CO_2 were simultaneously produced, around 510 K. As discussed above, the

Table 1
Experimental (thermogravimetry, TG) and theoretical weight losses of oxalate-precipitated materials (OC-series).

Material [a]	T_{max} (K) [b]	TG weight loss (wt%)	
		Experimental	Theoretical [c]
OC-CeD	396	17	16.6
	628	53	52.7
OC-ZnCe1D	370	8	10
	414	17	17
	653	52	51
OC-ZnD	413	18	19
	663	58	57

[a] Vacuum dried (323 K, 30 h) prior to heating/decomposition in synthetic air.
[b] DSC peak maxima.
[c] As per Scheme 1.

composite precursor showed an IR decomposition pattern closer to the one observed in the CC-Ce sample.

3.2.2. Gaseous products from the support precursors upon heating (TPO-MS)

Fig. 8 shows the m/e signals of H_2O, CO and CO_2 release, together with O_2 consumption, during dehydration and carbonate decomposition in synthetic air of the dry CC powders. The evolution of the H_2O and CO_2 mass signals supports the previous TG, DSC and TPO-IR assignments, namely: (i) the three successive water peaks in CC-CeD, at 340 (shoulder), 358 and 415 K, correspond to the stepwise dehydration of $Ce_2(CO_3)_3 \cdot 6H_2O$ and the following release of CO_2 (at approximately 550 K) indicates carbonate decomposition, (ii) zinc(II) hydroxycarbonate dehydroxylates/decomposes in a single step, jointly releasing H_2O and CO_2 at 510 K, and (iii) the CC-ZnCe1D composite releases first the crystallization water of cerium(III) hydroxycarbonate (~350 K) and, later, the coprecipitated zinc(II) hydroxycarbonate releases water (~493 K), with the final decomposition of cerium carbonate (CO_2 evolution) at 545 K.

In the CC-ZnD precursor, the observed intensity ratio of the m/e = 44 and m/e = 18 signals (CO_2/H_2O = 0.66) was consistent with the one expected for the decomposition of $Zn_5(OH)_6(CO_3)_2$ to ZnO, instead of that of the $Zn_4CO_3(OH)_6 \cdot H_2O$ decomposition (CO_2/H_2O = 0.25). Therefore, the formation of the latter precipitate was disregarded.

Zinc(II)hydroxycarbonate released CO_2 at lower temperature (~30 K) than cerium(III) carbonate, revealing less stability of the former. In particular, the CO_2 trace of the CC-ZnCe1D precursor showed that the decomposition of each carbonate appeared in consecutive steps. The peculiar features of the H_2O and CO_2 traces in this composite (evolution in consecutive steps and shifts to lower temperatures with respect to the pure materials, CC-CeD and CC-ZnD) suggest an intimate contact between the particles of both cerium(III) and zinc(II) carbonates.

Lastly, it is worth mentioning that a negligible consumption of molecular oxygen (m/e = 32), at 540 K, was recorded during the decomposition of the dehydrated $Ce_2(CO_3)_3$, in agreement with its oxidation to CeO_2 via the release of 3 mol of CO_2, while the CC-ZnD precursor evolved with no oxygen uptake. The composite, CC-ZnCe1D, exhibited just a minor O_2 consumption, due to the oxidation of Ce(III) to Ce(IV). No CO signal was observed in these CC-type precursors, indicating that the decomposition of the hydroxycarbonates proceeded releasing only CO_2 and water.

The combined analysis and correlation of the different thermal evolutions due to the decomposition in air of the materials prepared via the
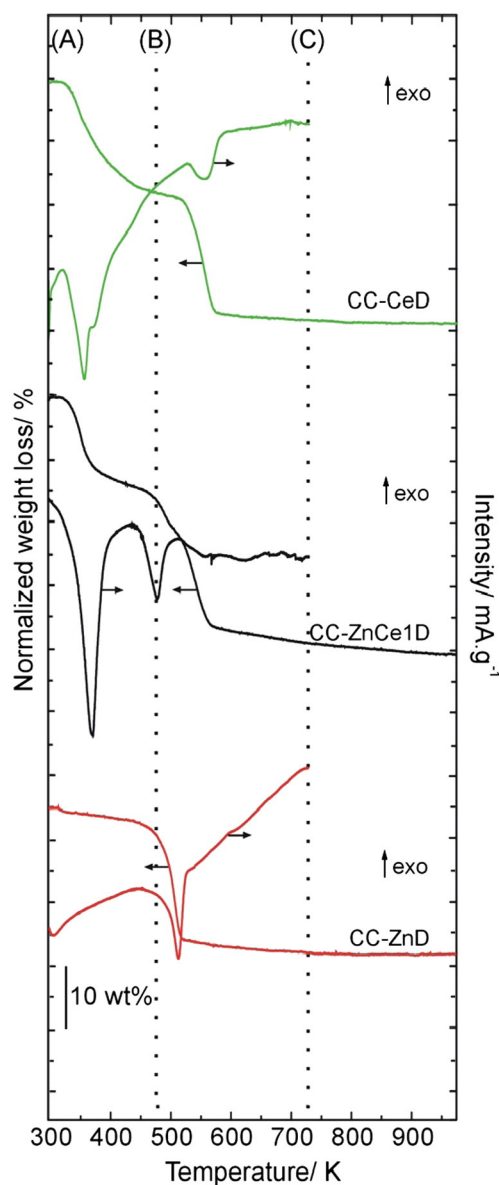
Fig. 5. Thermogravimetry and differential scanning calorimetry (TG and DSC) of the carbonate-precipitated (CC) powders, vacuum dried at 323 K: (——) CC-CeD, (——) CC-ZnCe1D, and (——) CC-ZnD.

Fig. 6. X-ray diffractograms of the carbonate-precipitated powders (——) CC-Ce, (——) CC-ZnCe1, and (——) CC-Zn: (A) dried at 323 K, (B) decomposed at 473 K, and (C) calcined at 723 K(under synthetic air).
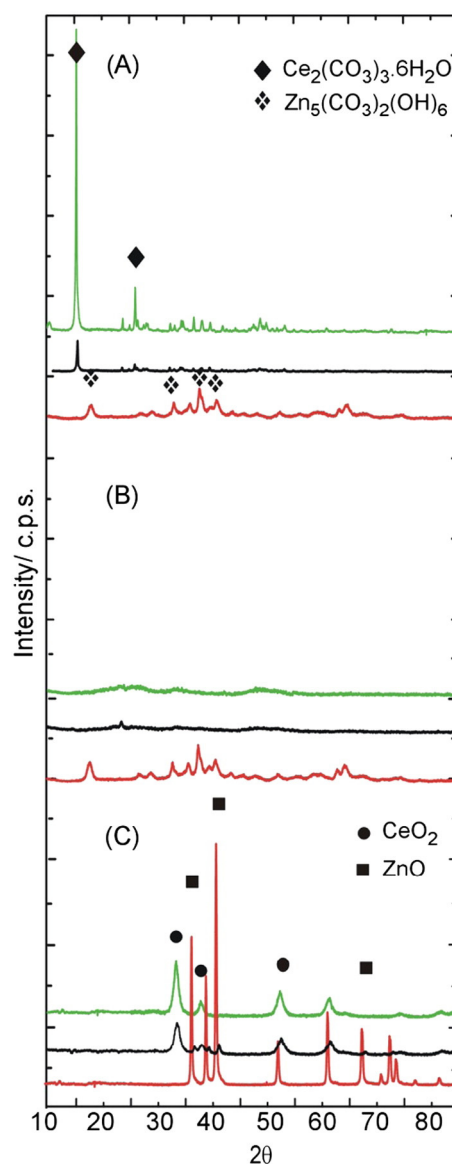
CC method suggest the global reactions indicated in Scheme 2. Table 2 compares the experimental and theoretical weight losses of these CC-type supports, for the proposed decomposition scheme, showing an excellent agreement between them.

3.3. Nanostructural and morphological characterization of the oxide powders

All the oxide materials (supports), calcined at 723 K, were further characterized prior to impregnating them with the palladium salt, to gain more insight on their morphological and structural features, aiming to relate these properties to the catalysts' performance.

3.3.1. X-ray diffraction

The previous study, with regard to the decomposition of the support precursors, suggested that the CC preparation method provided ZnO–CeO_2 nanocomposite powders where ZnO was probably more disperse and amorphous, and in more intimate contact with the nanometric CeO_2 crystals than in the ones produced by the OC method. Despite

our efforts to obtain high resolution electron microscopy images to analyze the material structures at the nanometric level, the low contrast between both oxides (CeO_2 and ZnO) and the low crystallinity of ZnO in the composite materials calcined at 723 K precluded proving the previous conclusion by means of that technique. To check that hypothesis, then, a refined XRD analysis was undertaken instead, as detailed in the Experimental section. Figs. 9 and 10 show the diffractograms of the full set of supports, air calcined at 723 K, where only the individual peaks of ZnO and CeO_2, without any evidence of the formation of another phase or compound, were identified. Moreover, as the insets of Figs. 9 and 10 indicate, neither the position nor the intensity of the (111) diffraction peak of CeO_2 ever changed, which rules out the incorporation of the Zn(II) cations into the ceria lattice [22,23]. As expected from the difference between the charges and radii of the involved cations, Zn(II) is highly prevented to become part of the ceria lattice. More similar ionic radii (and/or charges) are necessary to have the chance to form, for example, mixed oxides or solid solutions, like in the case of the Zr(IV) and Ga(III) cations [22,24,25].

Grain sizes have been evaluated for a long time by many techniques, starting from the early Scherrer formula, which relates peak width with
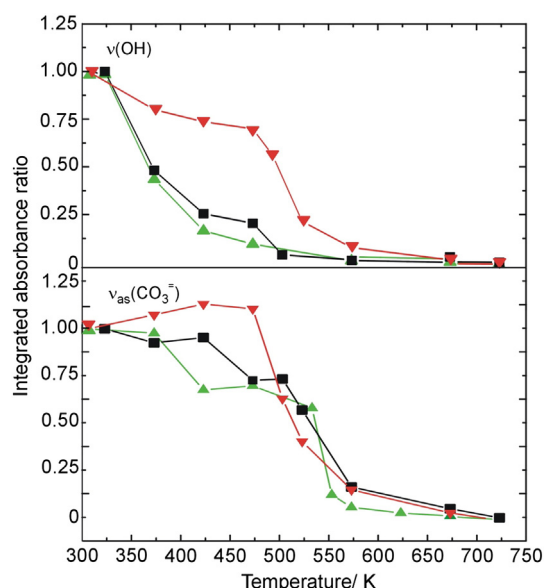
Fig. 7. Thermal evolution of the normalized integrated absorbance (transmission infrared) of the hydroxyl [ν(OH)] and carbonate [$\nu_{as}(CO_3^=)$] stretching bands of CC-CeD (▲), CC-ZnCe1D (■) and CC-ZnDC (▼), during temperature programmed oxidation (TPO-IR). The absorbance areas registered at 300 K were taken as reference, normalization values.

crystalline domain sizes [26]. Further developments and improvements allowed characterizing microstructure defects together with domains sizes (dislocation densities, stacking faults, twins, etc.). Williamson–Hall (W–H), Warren–Averbach (W–A) and Convolutional Multiple Whole Profile (CMWP) techniques are among the most well developed ones [27–32]. Modern Rietveld analyses software admit the introduction of particular models in the evaluation. These techniques are inscribed on the approach of using whole pattern fitting methods, considering wide peaks, overlapping, simultaneous presence of two or more phases, among others, by introducing hard constraints on the peak fitting by using crystallography restraints and physical models for peak broadening analysis [17,33]. On poly-phase materials, volume fractions of each phase have also been successfully calculated by whole pattern fitting, and the presence of an amorphous phase is also usually calculated from diffraction data. However, the simultaneous presence of many of these effects together renders diffractograms that call for a careful analysis.

In this regard, our two-phase systems (ceria and ZnO) are "ill posed" in many aspects, namely:

a) Concerning X-ray absorption, the linear absorption factor µ is quite different for both phases: Almost 9 times larger for CeO_2 (24.07 mm^{-1}) in comparison with ZnO (2.74 mm^{-1}). Dealing with this disparity on absorption factors is quite difficult. Below certain limit of the product of µ by the characteristic grain size (less than 0.01) no correction is necessary, but that assumption is not appropriate whenever the distribution of both phases is not homogeneous. Besides (see below), some of our composites were just on the limit of that product [34,35].
b) Regarding data cleanness, the diffractograms show highly overlapped peaks, which preclude the application of regular W–H, W–A and CMWP techniques [17,31–33].
c) In respect to amorphism, neither CeO_2 nor ZnO presents crystalline peaks in the region of usual wide peaks (that is, around 20° for Cu Kα_{12}) shown by amorphous materials, which would allow utilizing the current techniques applied to semi-crystalline materials, such as pharmaceuticals, polymers, coatings or ceramics [36–39].

However, in a large number of our composites both phases exhibited very small grain sizes, for what it is to be expected that a large
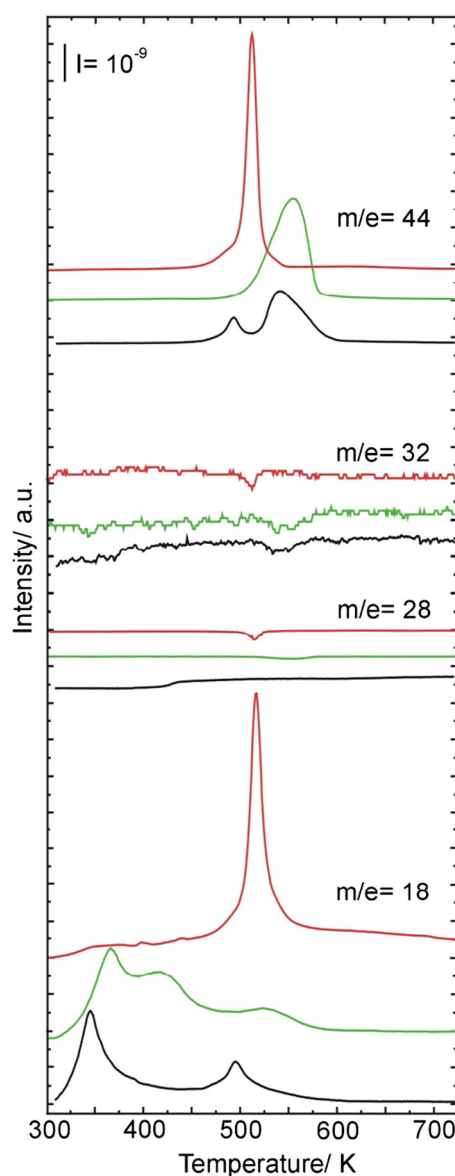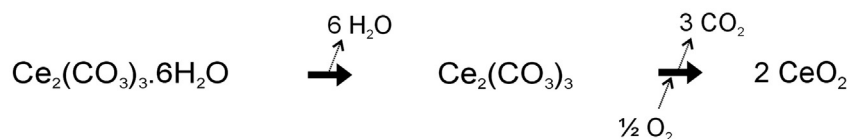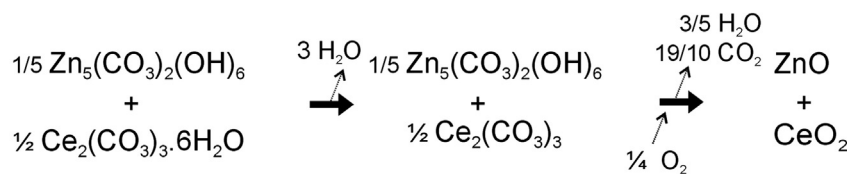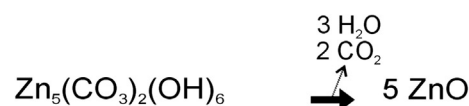

Fig. 8. Temperature programmed oxidation-mass spectroscopy (TPO-MS) patterns of the products of the CC materials under synthetic air: (—) CC-CeD, (—) CC-ZnCe1D, and (—) CC-ZnD.

proportion of their volume (that is, the surfaces of these high surface/volume ratio particles) certainly show amorphous behavior [40].

Single phase ZnO powders have been experimentally investigated before and their grain sizes were measured by using W–H analysis [41–43]. Yet, our two-phase systems were more complex and difficult to deal with. Table 3 shows crystallite sizes, that is, the sizes of the coherently scattering domains of the powders, as calculated by MAUD by the Delf model. The microdeformations were always negligible, with values < 10^{-4}, as expected for a ceramic material not subject to any kind of mechanical treatment. Stacking faults and twin volumes were not evaluated.

After calcination at 723 K, the sizes of the ceria crystals were rather constant (~10–15 nm) in all of the ZnO–CeO_2 nanocomposites, just as in the pure cerium oxide supports (OC-CeDC and CC-CeDC). However, the crystal size of the ZnO domains, which was somewhat similar in both pure ZnO supports (118 and 103 nm for OC-ZnDC and CC-ZnDC, respectively), was notoriously moderated by the presence of ceria: Both preparation methods yielded nanocomposite powders with ZnO domains smaller than those of the pure ZnO, being the lowest the values

CC-CeD

$$Ce_2(CO_3)_3.6H_2O \xrightarrow{6\ H_2O} Ce_2(CO_3)_3 \xrightarrow[\frac{1}{2}\ O_2]{3\ CO_2} 2\ CeO_2$$

CC-ZnCe1D

$$\begin{array}{c} \tfrac{1}{5}\ Zn_5(CO_3)_2(OH)_6 \\ + \\ \tfrac{1}{2}\ Ce_2(CO_3)_3.6H_2O \end{array} \xrightarrow{3\ H_2O} \begin{array}{c} \tfrac{1}{5}\ Zn_5(CO_3)_2(OH)_6 \\ + \\ \tfrac{1}{2}\ Ce_2(CO_3)_3 \end{array} \xrightarrow[\frac{1}{4}\ O_2]{\substack{3/5\ H_2O \\ 19/10\ CO_2}} \begin{array}{c} ZnO \\ + \\ CeO_2 \end{array}$$

CC-ZnD

$$Zn_5(CO_3)_2(OH)_6 \xrightarrow{\substack{3\ H_2O \\ 2\ CO_2}} 5\ ZnO$$

Scheme 2. Global reaction pathway of the CC-precipitates.

of the CC materials (31–38 and 57–78 nm for the CC and OC series, respectively), which suggest a better dispersion of the ZnO phase in these CC nanocomposites.
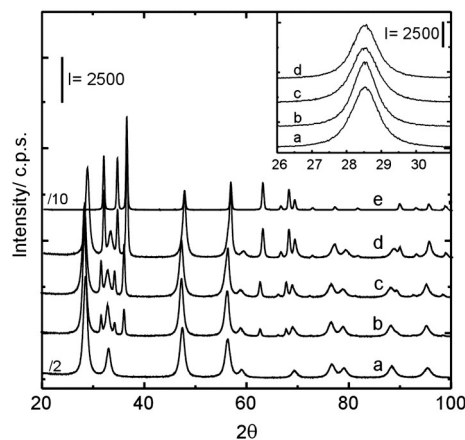
To assess whether this last feature would be preserved after more drastic experimental condition, the powders were re-calcined in air at 1173 K during 4 h. As a reference material, a mechanical mixture of the CeO_2 and ZnO powders, with a Zn/Ce atomic ratio equal to 1 (32.1 wt% ZnO), each of them prepared by the oxalate method, was also tested. The resulting crystal sizes are also shown in Table 3. Upon calcinations, the mechanical mixture (MM) had coherent crystalline domains of CeO_2 and ZnO similar to the ones obtained with the pure oxides (OC-CeDC and OC-ZnDC), respectively: (i) 14.2 vs. 13.5 nm (at 723 K) and 330.9 vs. 445.1 nm (at 1173 K) for ceria; and (ii) 174.4 vs. 117.9 nm (723 K) and 1224.8 vs. 644.9 nm (at 1173 K) for ZnO. As in the case of the MM reference sample, the growth of CeO_2 crystalline domains in the OC composites up to 1173 K was essentially not affected by the presence of ZnO in the composition (330.9 nm vs. 326.8–445.1 nm), but a contrasting situation was observed in the carbonate-derived composites (330.9 nm vs. 151.3–247.5 nm). In both sets of composites, after calcining at 1173 K, the larger the content of ZnO was, the smaller the final sizes of ZnO and CeO_2 domains became.

These results, which can be readily ascribed to mutual hindrance among the ZnO and ceria domains, precluding their crystal growth owing to the lack of available neighbors of the same phase material, also pinpoint to the good intimacy between both oxides achieved with both coprecipitation methods. Noteworthily, the final size of the ZnO

and CeO_2 crystalline domains in the oxalate-derived composites was always larger, up to 2-fold, than in the carbonate-derived ones. A better intimacy and dispersion of both oxide domains in the CC materials may account for this feature. Unhampered by the intimate mixture with CeO_2 grains, the ZnO domains grew to very large diameters on the MM sample upon calcining at 1173 K, reaching 1224.8 nm, the largest size of all inspected samples.

Fig. 11 shows the calculated (that is, XRD measurable — using the MAUD software) vs. the 'nominal' (that is the original composition of the materials) weight fractions of crystalline ZnO domains of each co-precipitated powders. X rays are sensitive only to the coherent domains (i.e., the crystalline phase) of any given component, remaining "blind" to the amorphous domains, except for their influence on the background intensity (microabsorption effects were also taken into account by the Vien model implemented in MAUD).

Mechanical mixtures of 100% crystalline ZnO and CeO_2 phases would give an exact fit between calculated and nominal weight fraction values. Instead, Fig. 11 shows a good fit for the ZnO + CeO_2 mechanical mixture only after re-calcining at 1173 K and reveals, instead, that the *relative* degree of crystallinity of the ZnO and CeO_2 grains after the calcination at 723 K was substantially different, the ceria grains being more amorphous than the zinc oxide particles were.

Table 2
Experimental (thermogravimetry, TG) and theoretical weight losses of carbonate-precipitated materials (CC-series).

Material [a]	T_{max} (K) [b]	TG weight loss (wt%)	
		Experimental	Theoretical [c]
CC-CeDC	373	18	19
	550	40	39.4
CC-ZnCe1DC	350	11	13.7
	488	18	21
	540	35	35.6
CC-ZnDC	505	21	25.8

[a] Vacuum dried (323 K, 30 h) prior to heating/decomposition in synthetic air.
[b] DSC peak maxima.
[c] As per Scheme 2.

Fig. 9. XRD patterns (5 s per 0.02° 2θ chopper increment) of the oxide powders obtained via the OC method (calcined at 723 K): a) OC-CeDC, b) OC-ZnCe05DC, c) OC-ZnCe1DC, d) OC-ZnCe2DC and e) OC-ZnDC.
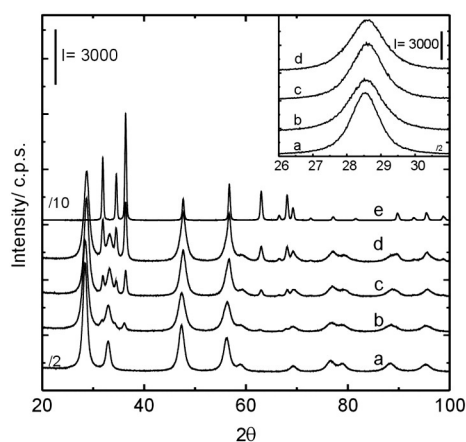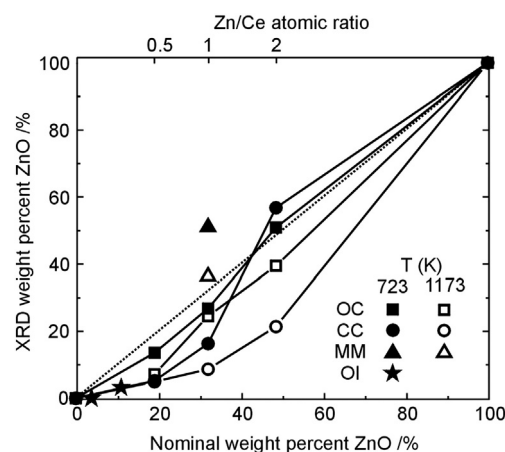
Fig. 10. XRD patterns (5 s per 0.02° 2θ chopper increment) of the oxide powders obtained via the CC method (calcined at 723 K): a) CC-CeDC, b) CC-ZnCe05DC, c) CC-ZnCe1DC, d) CC-ZnCe2DC and e) CC-ZnDC.

Fig. 11. Experimental (XRD measurable) vs. nominal weight fractions of crystalline ZnO in the co-precipitated materials: OC (square) and CC (circle), the ZnO-impregnated ceria (star), and the Zn/Ce = 1 at/at mechanical mixture OC (triangle), after air-calcining at the indicated temperatures.

Both series of composites calcined at 723 K were actually closer to the nominal ZnO wt% value than the corresponding re-calcined samples. Interestingly, whenever the Zn/Ce ratio was low (that is, whenever the coalescence of the ZnO grains was hampered by a comparatively much larger amount of the tiny ceria particles), the XRD-calculated ZnO wt% was lower than the nominal value while, conversely, the opposite was found for the largest Zn/Ce ratio. Regardless, the relative degree of crystallinity of ZnO in both series of nanocomposites after re-calcining at 1173 K dramatically decreased, thus revealing the less-constrained crystal growth of the smaller ceria grains of the powders.

A systematic evaluation of the amorphous content of each composite was not the purpose of the current work. Moreover, its evaluation by XRD would lack reliability because – as stated before – our materials befit in the worst case scenario of the most common amorphous phase evaluation techniques. The presence of nano-sized grains would preclude a correct evaluation of amorphous phases even if simultaneous peak broadening modeling were used on the Rietveld fit. Yet, MAUD allows for the inclusion of a few different peak broadening models, among which we have used the simplest one, known as the "Delf model" (other, more complex anisotropic models indicate the presence of the same phases). So, despite these difficulties we made a tentative appraisal of the presence of amorphous fractions by indirect ways, using the calculated values of the ZnO and CeO_2 crystalline domains and the 'mismatch' between the XRD estimates of the ZnO wt% vs. the corresponding nominal values of each material (shown in Fig. 11) to extract from

it (by just assuming that a disordered region is located around the crystalline domains of spherical particles of each oxide), the thickness ratio of said surrounding, disordered regions. Different grain shape assumptions give similar results. The thickness of the disordered surface region around each crystalline domain comprises a few cell parameters. Masoudi et al. [40] fixed an arbitrary value of 2 nm for their calculations but, nonetheless, the correct thickness of the surface-affected region remains unknown and can be different for both phases. They depend on the relative stability of the crystalline vs. the amorphous portions of two different oxides. Zhang and Banfield [44] found a value close to 3 nm for TiO_2 as the limit for amorphous phase becoming crystalline.

As described above, after calcining at 723 K the crystalline domains of CeO_2 in all samples exhibited a narrow size range, from 10 to 15 nm, with an average value of 13 nm for both preparation methods, which was also the value found in the pure cerias. The ZnO crystalline domains were somewhat larger in the CC co-precipitated composites, with an average of 35 nm, and even larger in the OC derived composites, with an average of 65 nm.

If, by assumption, the CeO_2 particles were surrounded by a 1.1 nm deep amorphous phase (i.e., close to 3 cell parameters), the ZnO particles would be amorphous until a depth of about 4 nm. Fig. 12 shows the resulting percent of amorphous phase for both ZnO and CeO_2. This schematic representation is in good agreement with the trends shown in Fig. 11 in regard to the weight fraction of ZnO. For instance, the

Table 3
Structural features of the OC, CC and OI powders, air-calcined at 723 K (and 1173 K).

Support	Crystal size [a] (nm)		S_{BET} [b] (m^2g^{-1})	V_p [c] (cm^3g^{-1})	d_p [d] (nm)
	ZnO	CeO_2			
OC-CeDC	–	13.5 (445.1)	67	0.10	6
OC-ZnCe05DC	77.7 (794.9)	14.9 (354.0)	49	0.09	8
OC-ZnCe1DC	56.8 (586.9)	13.0 (344.0)	53	0.11	9
OC-ZnCe2DC	58.2 (417.9)	14.5 (326.8)	40	0.11	10
OC-ZnDC	117.9 (644.9)	–	6	0.04	29
CC-CeDC	–	12.8	83	0.05	4
CC-ZnCe05DC	31.4 (504.1)	10.2 (247.5)	63	0.05	14
CC-ZnCe1DC	37.8 (406.9)	12.0 (169.1)	54	0.10	12
CC-ZnCe2DC	34.9 (283.6)	10.1 (151.3)	58	0.18	16
CC-ZnDC	102.7	–	8	0.06	38
MM [e]	174.4 (1224.8)	14.2 (330.9)			
OI-ZnCe04DC	67.1	14.0	52	0.08	6
OI-ZnCe1DC	182.4	14.2	48	0.08	6

[a] Estimated by XRD, with slow scans (5 s per 0.02° 2θ chopper increment) and high statistics measurement.
[b] BET (LN2) specific surface area.
[c] Pore volume.
[d] Barrett–Joyner–Halenda (BJH) pore diameter.
[e] Mechanical mixture of CeO_2 and ZnO (OC-CeDC and OC-ZnDC, respectively), Zn/Ce = 1 at/at.
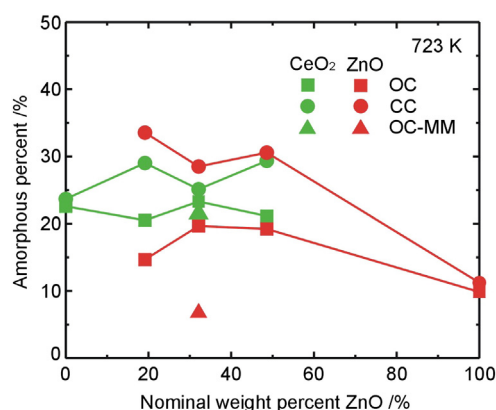
Fig. 12. Percent of amorphous phase for ZnO and CeO_2 in the different materials after air-calcining at 723 K. MM stands for mechanical mixture (see text).

amorphous portion of ZnO in both the pure oxide powders and the mechanical mixture is minimal while, owing to the small grain size of the CeO_2 grains, the amorphism of this phase is always higher than 20% in the nanocomposite materials.

A similar analysis performed with the re-calcined samples indicated – as expected – that the percent of amorphous phases became significantly lower for both ZnO and CeO_2, below 4% and 2%, respectively.

Finally the structure of the composite supports obtained by impregnating zinc nitrate onto ceria (OC-CeDC) was also analyzed by XRD. In the material with the smaller amount of zinc, OI-ZnCe04DC (nominal ZnO coverage = 0.42 at/at, 3.5 wt% ZnO) almost no ZnO diffraction peaks were observed (less than 1 wt% XRD-observable weight fraction; domain sizes = 67.1 nm) while the OI-ZnCe1DC sample (nominal ZnO coverage = 1.2, 11 wt% ZnO) showed ZnO crystalline domains of about 182.4 nm. The crystal size of CeO_2 was close to 14 nm in both materials, indicating that the re-calcination at 723 K of the ceria after the impregnation and decomposition of the zinc nitrate did not modify its morphology (Table 3). Both materials showed a relative ZnO crystalline content lower than that of their nominal values (Fig. 11), most likely owing to a significant interaction with the preformed ceria crystals.

3.3.2. Sorptometry

Adsorption/desorption LN2 isotherms were obtained for each of the oxide powders, calcined at 723 K (see Figs. 3S, 4S and 5S in Supplementary Information for the complete data). All of them gave Type II isotherms, typical of either non-porous (CC series) or macro-mesoporous solids (OC and OI series). This type of reversible isotherm is characteristic of unrestricted mono-multilayer adsorption [45]. In particular, the isotherms of the OC and OI supports exhibited the characteristic hysteresis due to capillary condensation in mesopores. Single-pore hysteresis prevailed in the OC-type materials.

Table 3 includes the specific surface area (S_{BET}), pore volume (V_p) and mean pore diameter (d_p) of the complete set of materials, calculated from the N_2 adsorption branch of each isotherm. In general, and in congruence with our XRD data, their pore size distribution indicated meso-macro porosity, with pore volumes between 0.04 and 0.18 cm^3 g^{-1}. The range of pore diameters in the materials was between 2 and 50 nm. These structural features allow forecasting the absence of steric hindrance.

Commercial ZnO has very low surface area (S_{BET} = 1–20 m^2 g^{-1}). In general, zinc oxides with high surface area have very poor thermal stability. Audebrand et al. made a detailed study of the structural properties of nanocrystalline ZnO powders produced by thermal decomposition of four different precursors (among them, hydrozincite and zinc oxalate) [41]. They showed that in all cases the crystal size and, also, the aspect (diameter-to-height) ratio of the crystallites increased with progressively higher calcining temperature. The aspect ratio was a strong

function of the precursor salt. The S_{BET} was always low, though, as it was in our OC-Zn and CC-Zn preparations.

The surface area of both ceria, OC-CeDC and CC-CeDC was about 10 times higher than that of the ZnO counterparts. Accordingly, the S_{BET} of the OC and CC nanocomposites was higher than the respective pure zinc oxides, OC-ZnDC and CC-ZnDC, the more so the higher the Ce content was (up to ~ 8-fold, from 6–8 to 53–63 m^2 g^{-1}). The OI supports had an intermediate surface area, close to that of the Zn/Ce = 1 co-precipitated composites.

We can conclude, then, that these OC, CC and OI preparation methods gave macro-mesoporous supports with moderate S_{BET}, and reasonable pore-related (i.e., V_p and d_p) values, which make them suitable for the study of the pursued catalytic reaction, the steam reforming of methanol (SRM). In particular, the substantial enhancement of the surface area of the zinc-containing nanocomposite powders, as compared with that of the pure ZnO, represents a remarkably encouraging feature with regard to catalytic performance of these materials, as detailed below.

3.4. Catalysts' performance

The performance of the full set of supported Pd catalyst in the steam reforming of an equimolar CH_3OH/H_2 mixture was evaluated between 400 and 650 K, at 0.1 MPa. Table 4 shows the temperature at which each catalyst reached 50% of methanol conversion, T_{50}, together with the respective selectivity to carbon dioxide, S_{CO2}, and water conversion, X_{H2O}, at said temperature.

These values clearly indicate that the Pd/CeO_2 catalysts were the most active (lowest T_{50} values), but that they mostly led to methanol decomposition (MD), as the selectivity to CO_2 was merely 9% in both of them. Conversely, although the Pd/ZnO catalysts were much less active (higher T_{50}), their selectivity toward the SRM reaction was the highest (S_{CO2} ~ 90%). The lower activity of the Pd/ZnO catalysts was, somehow, expected because of the small specific surface area of the zinc oxide supports (OC-ZnDC and CC-ZnDC), and that is why by means of its co-precipitation with ceria, or by impregnating ceria with $Zn(NO_3)_2$, larger available surface areas were sought after.

The nanocomposite-derived catalysts were very active as well. In particular, the Pd/OC-series catalysts were slightly more active than the Pd/CC analogs, and were progressively more selective to carbon dioxide the higher the Zn/Ce ratio was. Nevertheless, the S_{CO2} in the CC series was always better, reaching 78% in the Pd/CC-ZnCe05DC catalyst. About the same selectivity to CO_2 at T_{50} was observed in the Pd/OI-series, where only 1 wt% Pd loading was used. This suggests that the catalytic steps related to the metal function are not rate-determining.

At this point it is not yet clear why the OC-nanocomposite supports were less efficient to modulate the selectivity toward the SRM reaction than the CC-nanocomposite were.

Table 4
Performance of the supported Pd catalysts in the SRM reaction.[a]

Catalyst	T_{50} (K) [b]	S_{CO2} (%) [c]	X_{H2O} (%) [d]
Pd/OC-CeDC	489	10	4
Pd/OC-ZnCe05DC	505	51	26
Pd/OC-ZnCe1DC	507	48	25
Pd/OC-ZnCe2DC	512	67	33
Pd/OC-ZnDC	560	91	47
Pd/CC-CeDC	483	9	5
Pd/CC-ZnCe0.5 DC	521	78	38
Pd/CC-ZnCe1DC	513	73	37
Pd/CC-ZnCe2DC	525	63	32
Pd/CC-ZnDC	554	88	45
Pd/OI-ZnCe04DC	533	72	34
Pd/OI-ZnCe1DC	537	73	36

[a] P = 0.1 MPa; GHSV = 71500 cm^3 h^{-1} g^{-1}; W/F_{CH3OH}^o = 174 g h $m^{-3}$$_{CH3OH}$.
[b] Temperature at which X_{CH3OH} = 50%.
[c] Percent CO_2 selectivity (S_{CO2}) defined as: S_{CO2} = [$y_{CO2}/(y_{CO2} + y_{CO})$] × 100, at T_{50}.
[d] Percent H_2O conversion (X_{H2O}) defined as: X_{H2O} = [(F_{H2O}^{o} − F_{H2O})/F_{H2O}^o] × 100, at T_{50}.

It is likely that zinc oxide could be partially occluded by the ceria crystallites in the oxalate co-precipitated supports and/or that the higher ZnO crystals in these materials led to a smaller surface fraction of zinc oxide on them. This would imply a higher fraction of surface ceria and less interaction between palladium and zinc in the working OC-series catalysts. As a consequence, the somewhat higher activity found on Pd/OC-series was inexorably accompanied by lower CO_2 selectivity. In turn, the opposite situation could account for the CC-series. Whatever the ultimate reason might be, the Pd/CC-ZnCe05DC and Pd/OI-ZnCe0.4 DC composite catalysts were the best performing ones of the set.

4. Conclusions

Two co-precipitation methods were selected to obtain $ZnO–CeO_2$ nanocomposite powders: (1) an emulsion of dimethyloxalate in 1-hexanol, and $Ce(NO_3)_3$ and $Zn(NO_3)_2$ in aqueous phase, or (2) an addition of ammonium carbonate to the aqueous solution of the cerium(III) and zinc(II) nitrates, to yield the oxalate- (OC) or carbonate-derived (CC) precursors, respectively.

The hydrated Zn(III) and Ce(III) oxalates were first dehydrated to β-ZnC_2O_4 and $Ce_2(C_2O_4)_3$. Further, these oxalates were decomposed in an oxidizing atmosphere to ZnO and CeO_2, releasing particularly CO (from the zinc(II) salt), and CO_2. During this last step, O_2 consumption accompanied the oxidation of Ce(III) to Ce(IV). In the case of the carbonate-derived precursors, and after the dehydration of the cerium(III) carbonate, both of the remaining salts, $Zn_5(CO_3)_2(OH)_6$ (hydrocincite) and $Ce_2(CO_3)_3$, were decomposed to ceria, zinc oxide, CO_2 and water, with less O_2 demand than in the oxalate decomposition and oxidation of Ce(III) to Ce(IV). Moreover, the final decomposition of the oxalate salts took place at higher temperature than that of the carbonate-derived precursors (T_{max} was approximately 650 and 550 K for each type of nanocomposite, respectively).

In regard to the CC co-precipitated salts, another interesting feature appeared, as the combined mass, thermal and structural evolution results indicated that there was a higher dispersion of the zinc(II) carbonate in these nanocomposite powders than the one achieved following the OC method, which led to materials substantially different from those obtained by simple adding (mechanical mixture) the dry cerium(III) and zinc(II) pure (hydroxi)carbonates.

The structural characterization of the oxide materials, after calcination at 723 K, revealed the development of nanocrystalline domains of both ZnO and CeO_2. Although the ceria crystallite size was always within a narrow range (10–15 nm) for either the pure CeO_2 or the $ZnO–CeO_2$ nanocomposites, regardless of the preparation method or the zinc-to-cerium atomic ratio, the zinc oxide domains showed some dependence on both preparation parameters. The size of the ZnO crystallites on the pure oxides was about 110 nm, whereas the inclusion of ceria aided to the disintegration/fragmentation of such crystalline domains, which was higher for the carbonate-derived oxides (on average 35 vs. 65 nm for the CC resp. the OC series). In addition, the XRD-estimated ZnO weight percent, which lay below the nominal values, was indicative that some amorphous zinc oxide was also present in the nanocomposite powders. This amorphous fraction was higher in the CC-derived supports than in the OC ones. These combined observations revealed, consequently, that the dispersion of ZnO was decidedly superior in the carbonate-derived $ZnO–CeO_2$ nanocomposites.

The morphological features of all the oxides were also evaluated. The pure zinc oxides exhibited a low specific surface area (6–8 m^2g^{-1}), which increased noticeably with the addition of ceria (40–63 m^2g^{-1}). Thus, mesoporous composite powders with fair pore-related values ($V_p = 0.05–0.18$ cm^3g^{-1} and $d_p = 8–16$ nm) were obtained.

Finally, palladium was incorporated onto the surface of these active supports, and the resulting catalysts were employed in the methanol steam reforming reaction. It was shown that CeO_2 was responsible for the methanol decomposition reaction, that is, the undesirable production

of CO. However, whenever zinc oxide was part of the formulation, CO_2 selectivity was boosted and it became better the higher the dispersion of ZnO was. The Pd/CC-ZnCe catalysts yielded higher selectivity to carbon dioxide than their Pd/OC-ZnCe counterparts because in the first case higher palladium–zinc interaction was achieved.

Acknowledgements

Appendix A. Supplementary data

Supplementary data to this article can be found online at http://dx.doi.org/10.1016/j.powtec.2014.07.006.

References

[1] D.R. Palo, R.A. Dagle, J.A. Holladay, Methanol steam reforming for hydrogen production, Chem. Rev. 107 (2007) 3992–4021.
[2] M. Armbrüster, M. Behrens, K. Föttinger, M. Friedrich, E. Gaudry, S.K. Matam, H.R. Sharma, Synthesis and catalytic properties of nanoparticulate intermetallic Ga-Pd compounds, Catal. Rev. Sci. Eng. 55 (2013) 289–367.
[3] S. Sá, H. Silva, L. Brandao, J.M. Sousa, A. Mendes, Catalysts for methanol steam reforming — a review, Appl. Catal. B Environ. 99 (2010) 43–57.
[4] O. Ilinich, Y. Liu, C. Castellano, G. Koermer, A. Moini, R. Farrauto, A new palladium-based catalyst for methanol steam reforming in a miniature fuel cell power source, Platin. Met. Rev. 52 (2008) 134–143.
[5] Y. Suwa, S.-I. Ito, S. Kameoka, K. Tomishige, K. Kunimori, Comparative study between Zn-Pd/C and Pd/ZnO catalysts for steam reforming of methanol, Appl. Catal. A Gen. 267 (2004) 9–16.
[6] P. Pfeifer, A. Kölbl, K. Schubert, Kinetic investigations on methanol steam reforming on PdZn catalysts in microchannel reactors and model transfer into the pressure gap region, Catal. Today 110 (2005) 76–85.
[7] T. Conant, A.M. Karim, V. Lebarbier, Y. Wang, F. Girgsdies, R. Schlögl, A. Datye, Stability of bimetallic Pd–Zn catalysts for the steam reforming of methanol, J. Catal. 257 (2008) 64–70.
[8] F.J. Echave, O. Sanz, I. Velasco, J.A. Odriozola, M. Montes, Effect of the alloy on micro-structured reactors for methanol steam reforming, Catal. Today 213 (2013) 145–154.
[9] N. Iwasa, M. Yoshikawa, W. Nomura, M. Arai, Transformation of methanol in the presence of steam and oxygen over ZnO-supported transition metal catalysts under stream reforming conditions, Appl. Catal. A Gen. 292 (2005) 215–222.
[10] Q. Zhang, R.J. Farrauto, A PdZn catalyst supported on stabilized ceria for stoichiometric methanol steam reforming and hydrogen production, Appl. Catal. A Gen. 395 (2011) 64–70.
[11] C.R. Castellano, Y. Liu, A. Moini, G.S. Koermer, R.J. Farrauto, US patent 7,569,511B1 (August 4 2009).
[12] O.M. Ilinich, Y. Liu, E.M. Waterman, R.J. Farrauto, Kinetics of methanol steam reforming with a Pd–Zn–Y/CeO₂ catalyst under realistic operating conditions of a portable reformer in fuel cell applications, Ind. Eng. Chem. Res. 52 (2013) 638–644.
[13] L.A. Bruce, M. Hoang, A.E. Hughes, T.W. Turney, Surface area control during the synthesis and reduction of high area ceria catalyst supports, Appl. Catal. A Gen. 134 (1996) 351–362.
[14] Y. He, Nanostructured CeO₂ microspheres synthesized by a novel surfactant-free emulsion, Powder Technol. 155 (2005) 1–4.
[15] R.A. Young, The Rietveld Method, Int. Union of Crystallography, Oxford Science Publications, New York, USA, 1995.
[16] A.J. Guinier, Imperfection of crystal lattices as investigated by the study of x-ray diffuse scattering, Proc. Phys. Soc. 57 (1945) 310–324.
[17] L. Lutterotti, M. Bortolotti, IUCr: Compcomm Newsletter 1, L. Lutterotti, Trento, Italia, 2003. 43 (www.ing.unitn.it/~maud/facts.html).
[18] K.O. Hartman, The kinetics of oxalate ion pyrolysis in a potassium bromide matrix, J. Phys. Chem. 71 (1967) 392–396.
[19] J. Fujita, A.E. Martell, K. Nakamoto, Infrared spectra of metal chelate compounds. VI. A normal coordinate treatment of oxalate metal complexes, J. Chem. Phys. 36 (1962) 324–331.
[20] J.A. Goldsmith, S.D. Ross, Factors affecting the infrared spectra of some planar anions with D₃ₕ symmetry—III. The spectra of rare-earth carbonates and their thermal decomposition products, Spectrochim. Acta A 23 (1967) 1909–1915.
[21] M.C. Hales, R.L. Frost, Synthesis and vibrational spectroscopic characterization of synthetic hydrozincite and smithsonite, Polyhedron 26 (2007) 4955–4962.
[22] A. Trovarelli, Catalysis by ceria and related catalysts, Catalytic Science Series, vol. 2, Imperial College Press, London, 2002.
[23] D. Kim, Lattice parameters, ionic conductivities, and solubility limits in fluorite-structure MO₂ oxide (M = Hf⁴⁺, Zr⁴⁺, Ce⁴⁺, Th⁴⁺, U⁴⁺) solid solutions, J. Am. Ceram. Soc. 72 (1989) 1415–1421.
[24] S.E. Collins, G. Finos, E. Del Río, R. Alcántara, S. Bernal, A.L. Bonivardi, Effect of gallia doping on the acid–base and redox properties of ceria, Appl. Catal. A Gen. 388 (2010) 202–210.

[25] B. Bonnetot, V. Rakic, T. Yuzhakova, C. Guimon, A. Auroux, Preparation and characterization of $Me_2O_3 - CeO_2$ (Me = B, Al, Ga, In) mixed oxide catalysts. 2. Preparation by sol − gel method, Chem. Mater. 20 (2008) 1585–1596.

[26] P. Scherrer, Bestimmung der Grösse und der inneren Struktur von Kolloidteilchen mittels Röntgenstrahlen, Nachr. Ges. Wiss. Göttingen 26 (1918) 98–100.

[27] T. Ungár, J. Gubicza, G. Ribárik, A. Borbély, Crystallite size-distribution and dislocation structure determined by diffraction profile analysis: principles and practical application to cubic and hexagonal crystals, J. Appl. Crystallogr. 34 (2001) 298–310.

[28] T. Ungár, J. Gubicza, P. Hanák, I. Alexandrov, Densities and character of dislocations and size-distribution of subgrains in deformed metals by x-ray diffraction profile analysis, Mater. Sci. Eng. A 319 (2001) 274–278.

[29] B.E. Warren, X-ray Diffraction, Addison-Wesley, Reading, 1969.

[30] G. Ribárik, T. Ungár, Characterization of the microstructure in random and textured polycrystals and single crystals by diffraction line profile analysis, Mater. Sci. Eng. A 528 (2010) 112–121.

[31] Y.H. Dong, P. Scardi, MarqX: a new program for whole-powder-pattern fitting, J. Appl. Crystallogr. 33 (2000) 184–189.

[32] P. Scardi, M. Leoni, Diffraction line profiles from polydisperse crystalline systems, Acta Crystallogr. A 57 (2001) 604–613.

[33] P. Scardi, M. Leoni, Advances in line profile analysis for the study of nanocrystalline systems, ECS Trans. 3 (2006) 125–132.

[34] J.C. Taylor, C.E. Matulis, Absorption contrast effects in the quantitative XRD analysis of powders by full multiphase profile refinement, Appl. Crystallogr. 24 (1991) 14–17.

[35] B.M. Pederson, R.M. González, R.S. Winburn, Minimization of errors due to microabsorption or absorption contrast, Adv. X-ray Anal. 46 (2003) 68–73.

[36] B. Shah, V.K. Kakumanu, A.K. Bansal, Analytical techniques for quantification of amorphous/crystalline phases in pharmaceutical solids, J. Pharm. Sci. 95 (2006) 1641–1665.

[37] P.H. Hermans, A. Weidinger, Estimation of crystallinity of some polymer from X-ray intensities measurements, J. Polym. Sci. 4 (1949) 709–723.

[38] P.S. Prevéy, X-ray diffraction characterization of crystallinity and phase composition in plasma-sprayed hydroxyapatite coatings, J. Therm. Spray Technol. 9 (2000) 369–376.

[39] A. Benedetti, G. Cocco, G. Fagherazzi, B. Locardi, S. Meriani, X-Ray diffraction methods to determine crystallinity and preferred orientation of lithium di-silicate in Li–Zn-silicate glass ceramic fibers, J. Mater. Sci. 18 (1983) 1039–1048.

[40] M. Masoudi, M. Hashim, H.M. Kamari, M.S. Salit, A general method for quantifying the amorphous phase in nano polycrystalline materials, Mod. Appl. Sci. 6 (2012) 1–6.

[41] N. Auderbrand, J.-P. Auffrédic, D. Louër, X-ray diffraction study of the early stages of the growth of nanoscale zinc oxide crystallites obtained from thermal decomposition of four precursors. General concepts on precursor-dependent microstructural properties, Chem. Mater. 10 (1998) 2450–2461.

[42] D. Louër, J.P. Auffrédic, J.I. Langford, D. Ciosmak, J.C. Niepce, A precise determination of the shape, size and distribution of size of crystallites in zinc oxide by X-ray line-broadening analysis, J. Appl. Crystallogr. 16 (1983) 183–191.

[43] J.I. Langford, A. Boultif, J.P. Auffrédic, D. Louër, The use of pattern decomposition to study the combined X-ray diffraction effects of crystallite size and stacking faults in ex-oxalate zinc oxide, J. Appl. Crystallogr. 26 (1993) 22–23.

[44] H. Zhang, J.F. Banfield, Kinetics of crystallization and crystal growth of nanocrystalline anatase in nanometer-sized amorphous titania, Chem. Mater. 14 (2002) 4145–4154.

[45] K.S.W. Sign, D.H. Everett, R.A.W. Haul, L. Moscou, R.A. Pierotti, J. Rouquérol, T. Siemieniewska, Reporting physisorption data for gas/solid systems with special reference to the determination of surface area and porosity, Pure Appl. Chem. 57 (1985) 603–619.